

# Polar diatomic molecules in optical cavities: Photon scaling, rotational effects, and comparison with classical fields

Cite as: J. Chem. Phys. **154**, 094120 (2021); <https://doi.org/10.1063/5.0037995>

Submitted: 19 November 2020 . Accepted: 07 February 2021 . Published Online: 03 March 2021

 Johan F. Triana, and  José Luis Sanz-Vicario



View Online



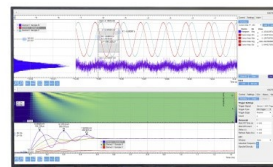
Export Citation



CrossMark

## Challenge us.

What are your needs for  
periodic signal detection?



Zurich  
Instruments



# Polar diatomic molecules in optical cavities: Photon scaling, rotational effects, and comparison with classical fields

Cite as: J. Chem. Phys. 154, 094120 (2021); doi: 10.1063/5.0037995

Submitted: 19 November 2020 • Accepted: 7 February 2021 •

Published Online: 3 March 2021



Johan F. Triana<sup>1</sup> and José Luis Sanz-Vicario<sup>2,a)</sup>

## AFFILIATIONS

<sup>1</sup>Department of Physics, Universidad de Santiago de Chile, Avenida Ecuador 3493, Santiago, Chile

<sup>2</sup>Grupo de Física Atómica y Molecular, Instituto de Física, Facultad de Ciencias Exactas y Naturales, Universidad de Antioquia UdeA, Calle 70 No. 52-21, Medellín, Colombia

**Note:** This paper is part of the JCP Special Topic on Polariton Chemistry: Molecules in Cavities and Plasmonic Media.

**a)** Author to whom correspondence should be addressed: [jose.sanz@udea.edu.co](mailto:jose.sanz@udea.edu.co)

## ABSTRACT

We address topics related to molecules coupled to quantum radiation. The formalism of light–matter interaction is different for classical and quantum fields, but some analogies remain, such as the formation of light induced crossings. We show that under particular circumstances, the molecular dynamics under quantum or classical fields produce similar results, as long as the radiation is prepared as a Fock state and far from ultra-strong coupling regimes. At this point, the choice of specific initial Fock states is irrelevant since the dynamics scales. However, in realistic multistate molecular systems, radiative scaling may fail due to the presence of simultaneous efficient non-radiative couplings in the dynamics. Polar molecules have permanent dipoles, and within the context of the full quantum Rabi model with a Pauli–Fierz Hamiltonian, they play a crucial role in the polaritonic dynamics since both permanent dipole moments and self-energy terms produce drastic changes on the undressed potential energy surfaces at high coupling strengths. We also gauge the effect of including rotational degrees of freedom in cavity molecular photodynamics. For diatomic molecules, the addition of rotation amounts to transform (both with classical or quantum fields) a light induced crossing into a light induced conical intersection. However, we show that conical intersections due to molecular rotation do not represent the standard properties of well-known efficient intrinsic conical intersections inasmuch they do not enhance the quantum transition rates.

Published under license by AIP Publishing. <https://doi.org/10.1063/5.0037995>

## I. INTRODUCTION

The coupling of molecules to quantum radiation in optical cavities or plasmonic environments may bring new expectations in the molecular structure and photodynamics, with implications in their chemical reactivity that eventually lead to new concepts and paradigms in light–matter interaction. Molecular polaritonics has become a new established field that brings together quantum optics and quantum chemistry.<sup>1–8</sup> The quantum photodynamics of isolated molecules interacting with quantized modes of radiation in cavities has become a fundamental problem by itself. Normally, a strong coupling regime is reached for a large ensemble of  $N$  molecules due to the  $\sqrt{N}$  factor in the coupling,<sup>7,9–13</sup> but recent

experiments have found evidence of single-molecule strong coupling of isolated molecules placed between nanospheres and mirrors.<sup>14</sup> Full *ab initio* multistate photodynamical calculations for isolated molecules are affordable, but only a few attempts have been reported for small ensembles.<sup>15,16</sup> The collective behavior has been explored with simplified model Hamiltonians such as those of Dicke,<sup>17</sup> Tavis–Cummings,<sup>18</sup> or Holstein–Tavis–Cummings.<sup>1</sup> Despite their simplicity and the lack of accurate description of the inner structure of molecules, much of the molecular polaritonics is understood due to the sound physical contents of these models.

In this work, we solve the *ab initio* time dependent Schrödinger equation for the polariton molecular states, thus assuming a unitary time evolution. To meet the experimental realm of molecules

within cavities and other nanostructures, the introduction of cavity decay losses and scattering rates is a must, and increasing efforts are being conducted to take them into account,<sup>19–22</sup> which requires the solution of master equations of the open molecular quantum system subject to an environment (cavities, plasmonic nanoantennas, and photonic crystals). In this way, our simulations are valid for a short time dynamics for which inner molecular motions are coupled to the radiation field faster than any other dissipative mechanisms.

Without considering the molecular rotation, the radiation interacting with molecules produces light induced crossings (LICs) in diatoms and light induced conical intersections (LICIs) in polyatoms between different electronic states. If rotation is also included in diatoms, LICIs are also present. It happens to occur for both classical<sup>23–25</sup> and quantum radiation fields,<sup>5,26</sup> and they bring non-adiabatic radiative transitions similar to those non-radiative transitions due to the non-adiabatic couplings (NACs) beyond the Born–Oppenheimer approximation. Since LIC and LICI are present in both classical and quantum formulations for the radiation field, it is questionable whether the photodynamics in both cases produce similar transition rates. If one compares classical results<sup>24,27</sup> with quantum results,<sup>2,3</sup> one may have the misleading idea that there is little new with quantized radiation. The classical–quantum field analogy has been also briefly analyzed in LiF.<sup>28</sup> In fact, good comparison is possible under given circumstances of coupling strengths and according to the form of preparing quantum radiation states. We have recently shown<sup>29</sup> that although individual Fock states allows for straight comparisons with classical fields, coherent or squeezed states of light produce a more complex photodynamics, which cannot be reproduced by any classical field. Since our proposal to work on LiF molecule in cavities,<sup>29,30</sup> this polar molecule has become a standard benchmark in cavity multistate molecular photodynamics.<sup>28,31,32</sup> We also propose<sup>30</sup> that the non-adiabatic molecular effects are responsible to produce new photons inside the cavity, a sort of dynamical Casimir effect, which has been exploited more recently in photoisomerization processes<sup>33</sup> and by using LiF to introduce a new basis of polarized Fock states.<sup>32</sup>

In our previous work,<sup>30</sup> we used the Pauli–Fierz Hamiltonian for LiF inside a cavity (together with the molecular Hamiltonian, we will name it the full Rabi model in this work), but for the coupling strengths used there, the deviations from a Jaynes–Cummings model were minimal. Here, we study the differences brought to the cavity photodynamics when using a full (Pauli–Fierz) Rabi model and a Jaynes–Cummings Hamiltonian. In polar molecules, the presence of permanent dipoles may bring dramatic changes in the structure of light-dressed potentials (due to both transition moments<sup>34</sup> and the dipole self-energy term) and consequently in the dynamics. The self-energy dipole term emerges naturally from the  $\mathbf{p} \cdot \mathbf{A}$  minimal coupling Hamiltonian after a Power–Zienau–Woolley (PZW) unitary transformation. This term has been a source of controversy and discussion along the years and a subject in very recent works.<sup>35,36</sup> In the present work, we do not intend to add arguments to the formal discussion of its appropriateness, but we just provide an assessment on its effect at strong couplings from an *ab initio* molecular perspective.

Recently, the rotational degree of freedom has been added to LiF cavity photodynamics.<sup>28</sup> However, we show here that the

light-induced conical intersection created by incorporating the rotation angle does not present the same properties of an intrinsic conical intersection in polyatomic molecules (with their transitional enhancement). Rotation may be identified as a countereffect in the goal to increase the radiation mediated rates.

This paper is organized as follows: First, in Sec. II, we introduce the total field-molecule Hamiltonian. We introduce a two-state molecular model for a diatom using Morse potentials, with transition and permanent dipole moments with  $R$ -dependence. This model allows us to perform fast dynamic computations using ingredients, which are also present in realistic molecules that require full *ab initio* calculations. In our work, the quantum radiation is represented in coordinate space  $x$ , which implies to perform 2D- $(R, x)$  polariton photodynamic calculations [or 3D- $(R, x, \theta)$  calculations when the rotation is also included]. Photodynamics using classical fields (1D- $R$  calculation) and quantum fields [2D- $(R, \theta)$ ] is explored to assess the classical–quantum analogy for different coupling strengths. In Sec. III, we use the proposed molecular model to study classical–quantum analogy, the scaling with Fock states, and the effects due to permanent dipole moments and to the addition of molecular rotation. In Sec. IV, we present *ab initio* results in LiF that show the inner workings of the permanent dipoles in the photodynamics, as well as the effect from rotational and Fock scaling.

## II. THEORETICAL DESCRIPTION

The Hamiltonian for a molecule subject to the quantized radiation inside an optical cavity takes the form  $\hat{H} = \hat{H}_{\text{Mol}} + \hat{H}_{\text{Rad}}$ , where  $\hat{H}_{\text{Mol}}$  corresponds to the electro-nuclear Hamiltonian of the molecule. For a cavity with a single mode of frequency  $\omega_c$ , the  $p$ -polarized electric field operator  $\hat{E}_p = E_0^Q(\hat{a} + \hat{a}^\dagger)\hat{e}_p$ , with quantum amplitude  $E_0^Q = \sqrt{\frac{\hbar\omega_c}{V\epsilon_0}}$ , can be expressed in the coordinate representation using  $(\hat{a} + \hat{a}^\dagger) = \sqrt{\frac{2\omega_c}{\hbar}}\hat{x}$  to yield  $\hat{E}_p = \lambda\omega_c\hat{x}\hat{e}_p$ , where  $\lambda = \sqrt{\frac{2}{V\epsilon_0}}$  is the coupling strength with the field. Now, the Pauli–Fierz radiation Hamiltonian for the cavity radiation reads (see Refs. 5 and 32 and references therein)

$$\begin{aligned}\hat{H}_{\text{Rad}} &= \frac{1}{2}\hat{p}^2 + \frac{1}{2}\omega_c^2\left(\hat{x} + \frac{\lambda}{\omega_c}\hat{\mu}(R)\right)^2 \\ &= \frac{1}{2}\hat{p}^2 + \frac{1}{2}\omega_c^2\hat{x}^2 + \lambda\omega_c\hat{x}\hat{\mu}(R) + \frac{1}{2}\lambda^2[\hat{\mu}(R)]^2,\end{aligned}\quad (1)$$

where  $\hat{\mu}(R)$  corresponds to the electronic dipole moment of the molecule (with a dependence on the nuclear geometry  $R$ ). The term  $\lambda\omega_c\hat{x}\hat{\mu}(R)$  contains the dipole operator for both the cavity and the molecule, and the last term  $\frac{1}{2}\lambda^2[\hat{\mu}(R)]^2$ , named the dipole self-energy, does not involve the cavity dipole interaction  $\hat{x}$ . For the molecule, one usually relies on the Born–Oppenheimer approximation to first solve the electronic eigenvalue problem that yields a set of potential energy curves or surfaces  $\{V_i(R)\}$ , and then, the nuclear problem is solved for the motion within these potentials. For a diatomic molecule, the electro-nuclear Hamiltonian (with a reduced nuclear mass  $\mu$ ) is

$$\hat{H}_{\text{Mol}} = -\frac{\hbar^2}{2\mu} \frac{\partial^2}{\partial R^2} + \hat{V}(R) \quad (2)$$

and the total Hamiltonian can be recast in the form  $\hat{H} = \hat{H}_{\text{Eff-Mol}} + \hat{H}_{\text{Field}} + \hat{H}_{\text{Mol-Field}}$  as

$$\begin{aligned} \hat{H} = & \left[ -\frac{\hbar^2}{2\mu} \frac{\partial^2}{\partial R^2} + \hat{V}(R) + \frac{1}{2} \lambda^2 [\mu(R)]^2 \right] \\ & + \left[ \frac{1}{2} \hat{p}^2 + \frac{1}{2} \omega_c^2 \hat{x}^2 \right] + \lambda \omega_c \hat{x} \hat{\mu}(R). \end{aligned} \quad (3)$$

In this work, for a two state problem, we call the Pauli–Fierz Hamiltonian in Eq. (3) the *full quantum Rabi model*, which does not include the rotating wave approximation (RWA), and the dipole self-energy adds to the potential energy curve. The more usual Jaynes–Cummings two-state model in quantum optics<sup>37</sup> is derived after neglecting the dipole self-energy and implementing the RWA in the quantum case (eliminating the non-energy conserving terms). However, in this work, we will call the *Jaynes–Cummings model* to the Hamiltonian where both the dipole self-energy and the RWA are eliminated. When the field is classical, for instance, taking a cw harmonic function,  $E(t) = E_0^C \cos(\omega t)$ , the semiclassical Rabi model is described by the Hamiltonian

$$\hat{H}_{\text{Clas}} = \hat{H}_{\text{Mol}} - E_0^C \hat{\mu}(R) \cos(\omega t), \quad (4)$$

a quantum problem that cannot be solved analytically without the RWA. The dynamics of populations deviate from the well-known analytical solutions of the semiclassical Rabi model within the RWA<sup>37</sup> when the field strength  $E_0^C$  is large. In fact, one finds merging oscillations in the time-dependent populations due to the field frequency  $\omega$  along with Rabi oscillations due to the cavity interaction, with Rabi frequency  $\Omega_R = E_0 \cdot \mu(R)/\hbar$ . Different regimes may be found for  $\Omega_R > \omega$  and  $\Omega_R < \omega$ . For the quantized radiation, the standard Jaynes–Cummings Hamiltonian for two states  $|g\rangle$  and  $|e\rangle$  preserves the excitation manifolds when the RWA is implemented (i.e., the Hamiltonian is block-diagonal with blocks involving  $|g, n\rangle$  and  $|e, n+1\rangle$  states). If the RWA is not implemented, the previous blocks are coupled and the excitation manifolds are not preserved, a notorious effect when the coupling factor  $\lambda$  is large (strong and ultra-strong coupling regimes).

The interaction of molecules with light (both in classical and quantum cases) produces non-adiabatic effects such as the formation of light-induced crossings or light-induced conical intersections<sup>3,38</sup> between coupled molecular states, and they appear at those nuclear geometries where the energy difference between potential energy surfaces (PES) equals the light frequency ( $\omega$  in the classical case or  $\omega_c$  in the quantum case). Due to this analogy, there is a misconception on whether or not the quantum field may produce the same interaction effect on molecules as the classical field does. Some previous results in the literature<sup>2,3,24,27</sup> may contribute to this idea after comparing photodynamic results with classical and quantum fields. Actually, this should not be served as a controversy. For a quantized radiation, while the molecule could be prepared initially at the  $|g\rangle$  state, at the  $|e\rangle$  or as a superposition, the field could be also prepared as a single Fock state  $|n\rangle$  of a superposition

$|F\rangle = \sum_n C_n |n\rangle$ . Within a coupling regime, where the Jaynes–Cummings Hamiltonian is valid and with an initial state prepared with a single Fock state, for instance,  $|e, n\rangle$ , the whole dynamics is confined to the excitation manifold corresponding to the pair  $|e, n\rangle$  and  $|g, n+1\rangle$ . The quantum Rabi frequency is  $\Omega_R^Q(n) = 2 \frac{\mu E_0^Q}{\hbar} \sqrt{n+1}$ . Similarly, the semiclassical Rabi frequency is  $\Omega_R^C = \mu E_0^C/\hbar$ . Both dynamics must be equivalent if Rabi frequencies are the same in the classical and the quantum case [i.e.,  $\Omega_R^C = \Omega_R^Q(n)$ ]. Therefore, if the amplitude of the classical field  $E(t)$  is chosen to be  $E_0^C = 2E_0^Q \sqrt{n+1} = \lambda \sqrt{2\hbar\omega_c} \sqrt{n+1}$ , one obtains the same dynamic response. This no longer happens if the RWA fails or the dipole self-energy contributes for large values of  $\lambda$  in ultra-strong regimes.

Additionally, if the quantum field is prepared as a superposition of Fock states, a single quantum Rabi frequency  $\Omega_R^Q(n)$  with  $n$  photons cannot be extracted from the more complicate entangled polariton state and the counterpart with a classical field cannot be established. In a recent work<sup>29</sup> we showed that dynamic results obtained using coherent and squeezed states (large superpositions of Fock states) cannot be reproduced by a tailored classical field  $E(t)$ . In addition, in the quantum case, the interaction term  $\lambda \omega_c \hat{x} \hat{\mu}(R)$  contains two dipole operators,  $\hat{x}$  for the radiation states and  $\hat{\mu}$  for the molecular states, acting simultaneously. The effective dipole for  $\hat{x}$  strongly depends upon the specific form of the quantum state of light. Whereas Fock states are stationary and dipole matrix elements have a simple dependence on  $n$ ,  $\langle n|\hat{x}|n+1\rangle = \sqrt{\frac{\hbar}{2\omega_c}} \sqrt{n+1}$ , coherent states of radiation may exhibit large effective dipoles due to the excursions of these states to large coordinate values, making polariton transitions much stronger.

To gauge the relevance of the dipole self-energy and to clarify the comparison between classical and quantum fields, we introduce a simple two-state model for a diatomic molecule with permanent dipoles. The electronic ground state  $|g\rangle$  and the first excited state  $|e\rangle$  are represented by potential energy curves simulated with Morse potentials (see Fig. 1),

$$V_i(R) = D_i \left[ 1 - e^{-\alpha_i(R-R_i^{eq})} \right]^2 - E_i^0, \quad i = g, e, \quad (5)$$

with different equilibrium distances  $R_i^{eq}$  and dissociation energies  $D_i$ . In this model, we assume that other electronic states are located much higher up in energy, and their participation in the photodynamics is negligible.

In Fig. 1, we indicate (on the molecular side) the expected polariton dynamics for this two-state molecular model. The vibrational ground state in the  $|g\rangle$  state is pumped up (with an intense laser pulse for instance) to the  $|e\rangle$  state with the potential curve  $V_e(R)$  so that we start the dynamics with a wave packet that is ready to move in the  $V_e(R)$  potential. To avoid the representation of the quantum field in terms of a large Fock basis  $\{|n\rangle\}$ , we choose instead to represent the quantum field in coordinate space.<sup>3,29</sup> It amounts to prepare the initial state as a molecular vibrational wave packet times a wave function for the quantum oscillator  $\phi_n(x)$  with mass unity. Then, the total time-dependent polariton state  $|\Psi(t)\rangle$  may be represented in the form  $\langle R, x|\Psi(t)\rangle = \phi_g(R, x, t)|g\rangle + \phi_e(R, x, t)|e\rangle$ , where  $\phi_i(R, x, t)$  represents the portion of the photon-molecule polariton wave packet for the

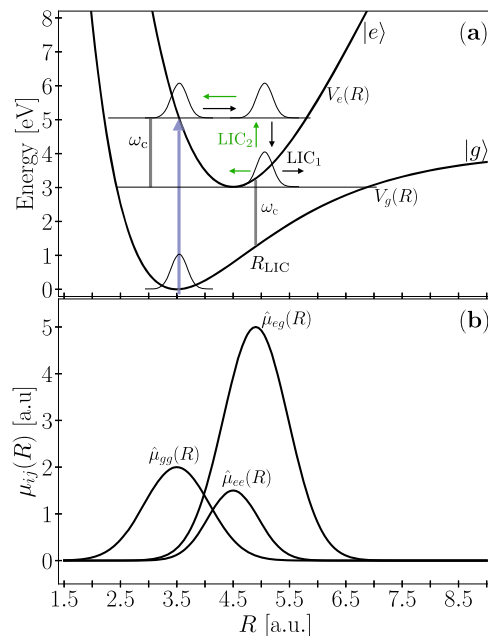


**FIG. 1.** (a) Potential energy curves  $V_i(R)$  represented with Morse functions of Eq. (5) for the electronic ground state ( $i = g$ ) and the first excited state ( $i = e$ ). For the ground state,  $D_g = 0.15$ ,  $\alpha_g = 0.58$ ,  $R_g^{eq} = 3.5$ , and  $E_g^0 = 0.0$ . For the excited state,  $D_e = 0.85$ ,  $\alpha_e = 0.27$ ,  $R_e^{eq} = 4.5$ , and  $E_e^0 = 0.11$ . (b) Electronic permanent ( $\hat{\mu}_{gg}$  and  $\hat{\mu}_{ee}$ ) and transition ( $\hat{\mu}_{ge}$ ) dipoles modeled with a Gaussian form,  $\mu_{ij}(R) = \Gamma_{ij} e^{-\sigma_{ij}(R-R_{ij}^{\mu})^2}$ . The permanent dipole for the ground state  $\hat{\mu}_{gg}$  makes use of parameters  $\Gamma_{gg} = 2.0$ ,  $\sigma_{gg} = 1.5$ , and  $R_{gg}^{\mu} = 3.5$ ; the permanent dipole for the excited states is modeled with  $\Gamma_{ee} = 1.5$ ,  $\sigma_{ee} = 2.5$ , and  $R_{ee}^{\mu} = 4.5$ ; the transition dipole moment uses  $\Gamma_{ge} = 5.0$ ,  $\sigma_{ge} = 1.5$ , and  $R_{ge}^{\mu} = 4.9$  (all quantities in atomic units).

vibrational  $R$  and cavity photon  $x$  coordinates, evolving in the effective potential associated with the  $i = g, e$  states. With this ansatz for the total polariton wave packet, we solve the time-dependent Schrödinger equation (TDSE)  $(\hat{H} - i\hbar \frac{\partial}{\partial t})|\Psi(t)\rangle = 0$ . In the basis of two electronic states, the total Hamiltonian in Eq. (3) can be represented in matrix form as

$$\hat{H}_{\text{Eff-Mol}} = -\frac{\hbar^2}{2\mu} \frac{\partial^2}{\partial R^2} \cdot \mathbf{1} + \begin{pmatrix} V_g(R) + \frac{1}{2}\lambda^2[\hat{\mu}(R)]_{gg}^2 & \frac{1}{2}\lambda^2[\hat{\mu}(R)]_{ge}^2 \\ \frac{1}{2}\lambda^2[\hat{\mu}(R)]_{ge}^2 & V_e(R) + \frac{1}{2}\lambda^2[\hat{\mu}(R)]_{ee}^2 \end{pmatrix}, \quad (6)$$

$$\hat{H}_{\text{Field}} = \left( -\frac{1}{2} \frac{\partial^2}{\partial x^2} + \frac{1}{2} \omega_c^2 x^2 \right) \cdot \mathbf{1}, \quad (7)$$

$$\hat{H}_{\text{Mol-Field}}^I = \begin{pmatrix} \lambda\omega_c x \mu_{gg}(R) & \lambda\omega_c x \mu_{ge}(R) \\ \lambda\omega_c x \mu_{ge}(R) & \lambda\omega_c x \mu_{ee}(R) \end{pmatrix}. \quad (8)$$

From this representation, it is clear that the polariton wave packet moves within 2D- $(R, x)$  surfaces, i.e., in the potential energy surfaces

$V_i(R) + \frac{1}{2}\lambda^2[\mu(R)]_{ii}^2 + \frac{1}{2}\omega_c^2 x^2 + \lambda\omega_c x \mu_{ii}(R)$  (for  $i = g, e$ ), with population transfer between these surfaces due to the off-diagonal interaction term  $\lambda\omega_c x \mu_{ge}(R)$ . The two diagonal terms of the dipole  $\lambda\omega_c x \mu_{ii}(R)$  and the dipole self-energy  $\frac{1}{2}\lambda^2[\mu(R)]_{ii}^2$  depend on the interaction coupling  $\lambda$ , and they contribute notoriously to the topology of the potential surfaces for large values of  $\lambda$ . Specifically, at variance with the dipole self-energy, the diagonal dipole term produces asymmetries of the potential along the field direction  $x$ .

### A. Computational method

To perform the dynamic calculations, the solution of the time-dependent Schrödinger equation (TDSE) is implemented using the multiconfigurational time-dependent Hartree (MCTDH) method.<sup>39–42</sup> The nuclear degree of freedom  $R$  is defined on a sin-DVR primitive basis with  $N_R = 301$  grid points between 1.5 a.u. and 9.0 a.u. Similarly, the coordinate corresponding to the cavity mode  $x$  is described by harmonic oscillator-DVR primitive basis functions with  $N_x = 251$  grid points between  $-25.0$  a.u. and  $+25.0$  a.u. If the rotational degree of freedom  $\theta$  is also included, the angular functional space is defined with a Legendre-DVR basis using  $N_\theta = 271$  grid points with magnetic rotational quantum number equal zero and using different partial waves ( $j_\theta$  values) to reach convergence. Thus, the total nuclear wave function  $\psi(R, x, \theta, t)$  reads

$$\psi(R, x, \theta, t) = \sum_{j_R=1}^{n_R} \sum_{j_x=1}^{n_x} \sum_{j_\theta=1}^{n_\theta} A_{j_R j_x j_\theta}(t) \phi_{j_R}^{(R)}(R, t) \phi_{j_x}^{(x)}(x, t) \phi_{j_\theta}^{(\theta)}(\theta, t), \quad (9)$$

where  $n_R = n_x = n_\theta = 20$  is the number of single particle functions  $\phi_{j_f}^{(f)}$  employed for each coordinate. We use a reduced mass  $\mu = 7430.0$  a.u. in this molecular model.

### III. RESULTS: MOLECULAR MODEL

Figure 1 indicates that the molecular wave packet evolves within the  $V_e$  potential curve (with an energy given by the Frank-Condon rule of vertical transition). The cavity produces a light-induced crossing (LIC) at the internuclear distance  $R_{\text{LIC}} = 4.9$  a.u. where  $\hbar\omega_c = V_e(R) - V_g(R)$ . When the polariton wave packet reaches this LIC area [where the transition dipole  $\mu_{ge}(R)$  has its maximum strength], part of the wave packet transfer to the  $V_g(R)$  curve with the emission of one cavity photon with energy  $\hbar\omega_c$  (we call it LIC<sub>1</sub> transition). Similarly, the new wave packet created within the  $V_g$  potential may eventually transfer up to the  $|e\rangle$  state when it approaches the LIC area (we call it LIC<sub>2</sub> transition). However, the approximate periodic motion of a wave packet in  $V_g$  at  $E \sim 3$  eV is much longer than that of a wave packet in  $V_e$  with energy  $E \sim 5$  eV.

The polariton wave packet passes across the LIC region every 20 fs. This periodic behavior is observed in Fig. 2: the population of the ground state is fed every 20 fs due to the LIC<sub>1</sub>, a robust effect for any value of  $\lambda$  in display from  $\lambda = 0.001$  to 0.03. For a weak coupling ( $\lambda = 0.001$ ), the upper state is being monotonically depopulated by the LIC<sub>1</sub> interaction. For  $\lambda = 0.005$ , we already reach a strong coupling, and along with the depopulation of the upper state, the  $|e\rangle$



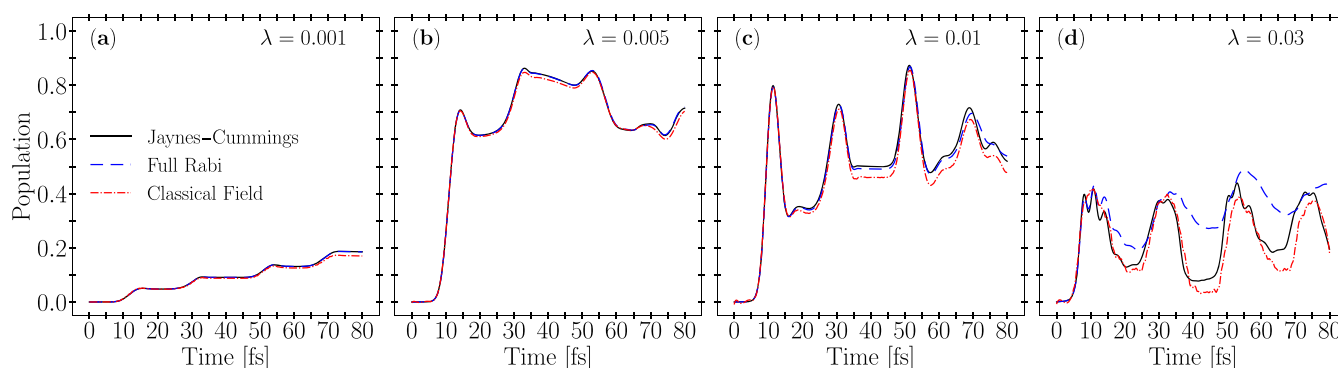


**FIG. 2.** Time evolution of the polariton population corresponding to the ground state  $|g\rangle$  [wave packet  $\phi_g(R, x, t)$ ] with an initial condition set at the  $V_g$  potential in the form  $\phi_{v=0}^{V_g}(R) \times \phi_{n=0}(x)$ . Simulations include the results obtained with the full Rabi model, the Jaynes–Cummings model (without RWA) and with a classical field  $E(t)$  for different radiative coupling strengths: (a)  $\lambda = 0.001$  a.u., (b)  $\lambda = 0.005$  a.u., (c)  $\lambda = 0.01$  a.u., and (d)  $\lambda = 0.03$  a.u. and for a cavity mode frequency  $\omega_c = 2$  eV.

state recovers part of the population when the polariton wave packet  $\phi_g(R, x, t)$  within the  $V_g$  potential reaches the LIC area after returning from the turning point at  $R \sim 7$  a.u. (LIC<sub>2</sub> process). This mutual nutrition across the LIC is much more evident for  $\lambda = 0.01$  with plateaux where both wave packets are still far from the LIC region. For coupling strengths below  $\lambda = 0.01$ , the results obtained with the full Rabi model, with the Jaynes–Cummings model and with a classical field, are basically the same. For an ultrastrong coupling regime ( $\lambda = 0.03$ ), the results deviate notoriously. At this stage, the dipole self-energy term is able to modify the potential energy surfaces, and this potential modification is the only cause for the difference between the full Rabi Hamiltonian and the Jaynes–Cummings Hamiltonian in our molecular model.

The result with the classical field approximately follows the result of the Jaynes–Cummings model. In this case, the small difference comes from the different dimensionality: whereas the classical case still remains as a 1D calculation of wave packets in the  $R$ -coordinate, the Jaynes–Cummings model is a 2D calculation ( $R, x$ ) with asymmetries in the  $x$  direction, which are enhanced for large values of  $\lambda$ . In addition, since the RWA is not implemented in our so-called *Jaynes–Cummings model*, for an ultrastrong coupling regime, the excitation manifold,  $\{|g, 1\rangle, |e, 0\rangle\}$ , is not preserved, and other higher excitation manifolds  $\{|g, n+1\rangle, |e, n\rangle\}$  for  $n > 0$  start to participate. These intruders cause that the above-mentioned equality  $E_0^C = 2E_0^Q\sqrt{n+1}$  be not fully satisfied. One also finds that inner oscillatory structures begin to appear for  $\lambda = 0.03$ . They are simply quantum Rabi-like oscillations with a period  $T = 2\pi/\Omega_R(n)$  that depends on  $\lambda$ . For  $\lambda = 0.001$ – $0.01$ , the time spent by the molecular wave packet close to the LIC area is shorter than the Rabi period [note also that the transition dipole function  $\hat{\mu}_{ge}(R)$  is not constant so that the effective action of the cavity radiation depends on a time window across the LIC]. For  $\lambda = 0.03$ , the period for the Rabi oscillation is around 3 fs, and it generates three Rabi oscillations during the time window of the LIC. These inner Rabi oscillations reduce the amplitude of the population exchange. The same Rabi oscillations can also be distinguished in the calculation with the classical field, but they are almost diluted in the case of the full Rabi model.

Here, we have used the vacuum  $|0\rangle$  as initial Fock state, and as long as the RWA is fulfilled, the only Fock states involved in the lowest excitation manifold are  $|0\rangle$  and  $|1\rangle$ . One may be tempted to use another initial Fock state  $|n\rangle$ . However, for weak and even strong coupling regimes ( $\lambda = 0.001$ – $0.01$ ), the results scale almost exactly. The changes in the coupling term  $\lambda\omega_c\hat{x}\hat{\mu}(R)$  may only come from the chosen value of  $\lambda$  and the dipole matrix element involved between two Fock states  $\langle n|\hat{x}|n+1\rangle$ . Clearly if one chooses a value of  $\lambda_0$  for the calculation involving the lowest excitation manifold  $\{|0\rangle, |1\rangle\}$ , the same result can be replicated with other  $\lambda_n$  values for higher excitation manifolds  $\{|n\rangle, |n+1\rangle\}$ , just using the scaling rule  $\lambda_0 = \lambda_n\sqrt{n+1}$ . This perfect matching in the populations for  $\lambda = 0.001, 0.005$ , and  $0.01$  is not shown in Fig. 2 since they are indistinguishable curves. Therefore, there is no new physics as long as the excitation manifolds are not strongly mixed. For instance, this scaling starts to fail for higher values of  $\lambda_0$ , like  $\lambda_0 = 0.03$  or  $0.04$  (see Fig. 3), just by using the Jaynes–Cummings model, and the comparison is even worse with the full Rabi model (not shown). For  $\lambda_0 = 0.04$  in Fig. 3, the dynamics initiated with the Fock states  $|n\rangle$  ( $n > 1$ ) clearly departs from that of the vacuum state  $|0\rangle$ . The excitation manifold  $\{|0\rangle, |1\rangle\}$  has no excitation manifold below, and it is the only excitation manifold below  $\{|1\rangle, |2\rangle\}$ . When  $n$  increases, the number of excitation manifolds below and above are similar, which explains the saturation of the population for higher  $n$  values, thus representing a kind of Fock scaling even when the RWA is not satisfied. Such scaling laws are much more elusive or even impossible for other quantum states of light expressed in terms of superpositions of Fock states (which should be norm and not the exception in current experiments).

### A. Rotational effects

Diatomic molecules can also rotate in the presence of the  $p$ -polarized quantum field of the cavity. This implies (in its more basic formulation) to include the interaction of the molecular dipole with the field that tends to align the dipole along the direction of the field. To upgrade our model, the molecular Hamiltonian now includes the centrifugal term

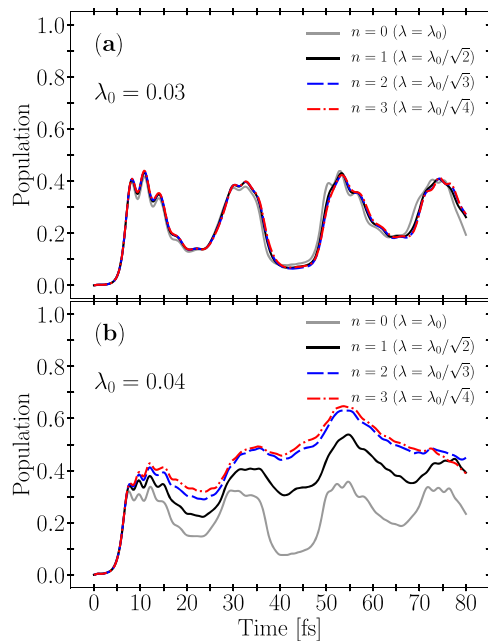


**FIG. 3.** Time evolution of the polariton population associated with the ground state  $|g\rangle$  using our Jaynes-Cummings Hamiltonian model (without RWA) for coupling parameters (a)  $\lambda_0 = 0.03$ , and (b)  $\lambda_0 = 0.04$ , and with the lowest photon excitation manifold  $\{|0\rangle, |1\rangle\}$  for  $\lambda_0$ . The plot also includes populations for scaled values  $\lambda_n = \lambda_0/\sqrt{n+1}$  using higher excitation manifolds  $\{|n\rangle, |n+1\rangle\}$ , respectively, for  $n = 1-3$ .

$$H_{\text{Mol}} = -\frac{\hbar^2}{2\mu} \frac{\partial^2}{\partial R^2} + \frac{\hat{J}^2}{2\mu R^2} + \hat{V}(R), \quad (10)$$

and dipole couplings now must include an orientation factor, i.e.,  $\lambda\omega_c \hat{x}\hat{\mu}(R) \cos\theta$ .

Accordingly, the polariton wave packet  $|\Psi(t)\rangle$  must include the rotational degree of freedom,

$$\langle R, x, \theta | \Psi(t) \rangle = \varphi_g(R, x, \theta) |g\rangle + \varphi_e(R, x, \theta, t) |e\rangle,$$

and single particle functions  $\phi_{j\theta}^{(\theta)}$  are conveniently added in the MCTDH ansatz. We may select different initial states  $|J, M\rangle$  for the rotational motion (we choose  $M = 0$  with dependence on  $\theta$  only). For the sake of simplicity, let us say that we employ a basis in the Dirac form  $|\{g, e\}, v, n, J, M = 0\rangle$  (the label  $v$  for the vibrational states, the label  $n$  for the Fock states, and labels  $J, M$  for the angular states). The transition dipole matrix element is factorized according to

$$\begin{aligned} \langle e, v, n, J, 0 | \lambda\omega_c \hat{\mu}(R) \cos\theta | g, v', n', J', 0 \rangle \\ = \lambda\omega_c \langle v | \hat{\mu}_{ge}(R) | v' \rangle \langle n | \hat{x} n' \rangle \langle J, 0 | \cos\theta | J', 0 \rangle. \end{aligned} \quad (11)$$

The transition matrix element in Eq. (11) is separated in electro-nuclear, cavity, and rotational angular terms. We have already

analyzed the scaling rule for different Fock states due to the form of the matrix element  $\langle n | \hat{x} | n' \rangle$ . The angular matrix element is analytical in terms of 3j-Wigner coefficients

$$\langle J, 0 | \cos\theta | J', 0 \rangle = \sqrt{(2J+1)(2J'+1)} \begin{pmatrix} J & 1 & J' \\ 0 & 0 & 0 \end{pmatrix}^2. \quad (12)$$

The addition of the angular degree of freedom  $\theta$  causes the presence of light-induced conical intersections (LICIs) instead of light induced crossings (LICs) (see, for example Ref. 43). It may be though that 3D LICs, in general, are much more efficient than 2D LICs both with classical or quantum radiation fields. However, at variance with other nuclear degrees of freedom, we find that this is not the case with molecular rotation in diatomics. Since  $|\langle J, 0 | \cos\theta | J', 0 \rangle| < 1$  for any  $J, J'$  pair, this angular factor makes 3D transition probabilities to show lesser oscillator strengths than 2D transitions, an effect that can be appreciated in Fig. 4, where the 2D- $(R, x)$  probabilities lie above the 3D- $(R, x, \theta)$  probabilities for a set of different angular initial conditions  $J$ .

Whereas the Fock transition  $\langle e, n | \hat{\mu} \hat{x} | g, n' \rangle$  is limited to  $n' = n + 1$  because of the preservation of the excitation manifold for weak and strong couplings (or at least a dominant excitation manifold at short times for ultrastrong couplings where RWA fails and other

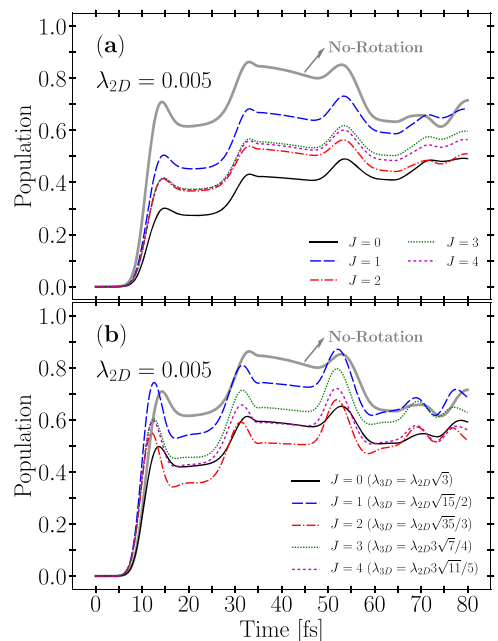


**FIG. 4.** (a) Time evolution of the polariton population associated with the ground state  $|g\rangle$  with the full Rabi model for a coupling  $\lambda_{2D} = 0.005$  for a 2D calculation (without rotation) and the same  $\lambda_{2D}$  for 3D calculations (including rotation) using different initial rotational states  $|J, 0\rangle$  (with  $J = 0, 1, 2, 3$  and 4). (b) Same as (a) with 3D calculations using the same initial rotational states but with scaled  $\lambda_{3D} = \lambda_{2D}/\langle J | \cos\theta | J' \rangle$ .

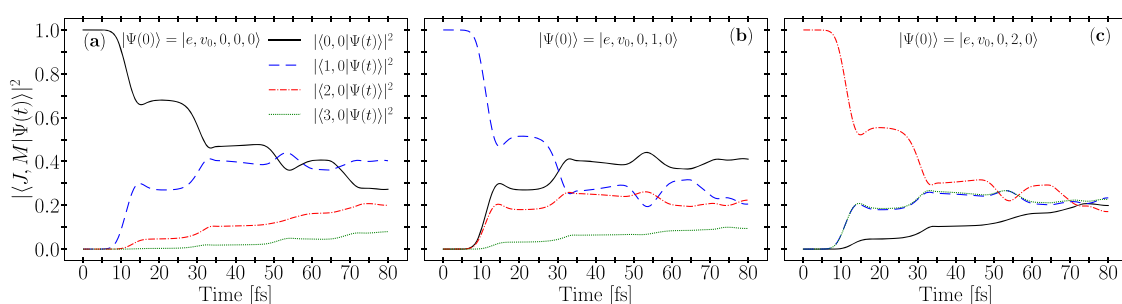


**FIG. 5.** Time evolution of the polariton population of the  $|\Psi(t)\rangle$  state projected on the  $|J, M\rangle$  angular components associated with both the ground state  $|g\rangle$  and the excited state  $|e\rangle$  when using different conditions in the angular function  $(|J, 0\rangle)$  with  $J = 0, 1, 2$ , and  $3$  in the  $|\Psi(t=0)\rangle = |e, v_0, n=0, J, M\rangle$  initial state. A coupling  $\lambda = 0.005$  is used in these simulations.

nonlinear effects appear), there is no such limitation for the angular transition  $J \rightarrow J' \pm 1$  and no  $J$ -excitation manifolds need to be preserved. In addition, transitions associated with different degrees of freedom may be in distinct time scales, which, in turn, depend on the specific form of the transition matrix element and the quantum labels involved ( $n$  or  $J$ ). Anyway, in this particular molecular model, the transitions due to the cavity happen to occur only within the time window in which the polariton density moves across the LIC or LIC1. Similarly to the Fock case, the initial angular state may be selected as a single  $|J, M\rangle$  state or as a superposition  $\sum_{J,M} C_{J,M} |J, M\rangle$ . In the latter case, rules of angular scaling fail. However, for a single  $|J, M\rangle$  angular state, one is tempted to test for some sort of scaling, according to Eq. (12).

Figure 4 contains results on time-dependent populations of the polariton associated with the ground state  $|g\rangle$  for different initial angular states  $|J, 0\rangle$  (with  $J = 0, 1, 2$ , and  $3$ ). The largest drop of population is for  $J = 0$  since from the start the only available transition is  $J = 0 \rightarrow J' = 1$  with a transition probability  $|\langle 0, 0 | \cos \theta | 1, 0 \rangle|^2 = 1/3$ . This factor approximately explains the comparison between the cases without and with rotation for short times because for subsequent times, one finds additional rotational transitions  $J' = 1 \rightarrow J'' = 2$  and  $J'' = 2 \rightarrow J''' = 3$  at each LIC1 crossing [see Fig. 5(a)], thus eliminating a general scaling rule for the whole propagation. Now, if we choose  $J = 1$  as the initial angular state, the population increases compared to the  $J = 0$  state; with  $J = 1$ , two final angular states are available:  $J' = 0$  with a probability branching ratio  $1/3 = 0.333$  and  $J' = 2$  with a branching ratio  $4/15 = 0.266$  [see Fig. 5(b)]. The opening of two angular channels from the start increases the transition probability. However, the probabilities for the two branching ratios tend to the same limit as  $J$  increases. For instance, if we choose initially  $J = 2$ , the branching ratio for  $J' = 1$  is  $4/15 = 0.266$  and for  $J' = 3$  is  $9/35 = 0.257$ , and both partial waves contribute almost equally [see Fig. 5(c)]. Finally, the results for  $J = 3$  and  $4$  are very similar to  $J = 2$  until  $t = 30$  fs in Fig. 4. Clearly, this behavior follows for larger  $J$  values because  $|\langle J, 0 | \cos \theta | J \pm 1, 0 \rangle|^2 = 1/4$  for  $J \rightarrow \infty$ . This saturation value in populations for high  $J$  is similar to that saturation for high  $n$  in the Fock scaling above mentioned. This limit for high  $J$  values precludes rotational motion from being a good candidate to explore enhancements in the population yields for some sort of radiation control in molecules.

#### IV. RESULTS: LiF MOLECULE

Here, we deal with a more realistic polar molecule, LiF, a diatomic molecule with permanent dipole moments. We also want to gauge in LiF the effect of the dipole self-energy term, scaling rules with different initial Fock states, and the introduction of the rotational degree of freedom. Full details on the electronic structure calculations performed with MOLPRO<sup>44</sup> (potential energy curves, dipole matrix elements, and non-adiabatic couplings) and the dynamic details using MCDTH closely follow those already reported in our previous work.<sup>29,30</sup> We reduce our calculations for the LiF system to the two lowest  $^1\Sigma$  states. The third lowest  $^1\Sigma$  state barely contributes at the cavity mode frequencies used (even for rather strong couplings) since the dipoles between the two lowest states and the third one are comparatively small at the internuclear distances of interest. In LiF, there is a feature not present in the molecular model introduced in Sec. II: an avoided (ionic-covalent) crossing between the two lowest  $^1\Sigma^+$  states with the corresponding non-adiabatic coupling (NAC) located at  $R_{\text{NAC}} = 13.1$  a.u. (see Fig. 6). It means that two transfer mechanisms are present: first, the radiative one due to the LIC generated at  $R_{\text{LIC}} = 6$  a.u. due to the cavity mode frequency used here  $\omega_c = 2.907$  a.u., and second, the non-radiative transfer due to the NAC at  $R_{\text{NAC}} = 13.1$  a.u. In this LiF system, we start the simulation by placing a wave packet in the dissociating excited state  $2^1\Sigma^+$  ( $|e\rangle$  state) [which is simply a Franck-Condon carbon copy of the ground vibrational state  $v = 0$  in the electronic ground state  $1^1\Sigma^+$  ( $|g\rangle$  state)], with energy  $E \sim 7$  eV.

The initial state in our polariton propagation corresponds to this non-stationary molecular state times a Fock state  $|n\rangle$  represented in coordinate space, with total energy  $E \sim 7 + \hbar\omega_c(n + 1/2)$ . The Hamiltonian in the TDSE also corresponds to that of Eq. (3) but supplemented here with the non-adiabatic couplings

$$C_{ij}(R) = -\frac{\hbar^2}{2\mu} [2\langle i | \partial / \partial R | j \rangle(R) \partial / \partial R + \langle i | \partial^2 / \partial R^2 | j \rangle(R)],$$

with  $i, j = g, e$ .<sup>29</sup> The polariton dynamics evolves in 2D- $(R, x)$  effective potential energy surfaces (PESs),  $V_i(R) + \frac{1}{2}\lambda^2[\dot{\mu}(R)]_{ii}^2 + \frac{1}{2}\omega_c^2 x^2 + \lambda\omega_c x \mu_{ii}(R)$ , or 3D- $(R, x, \theta)$  PES if rotation is also included (due



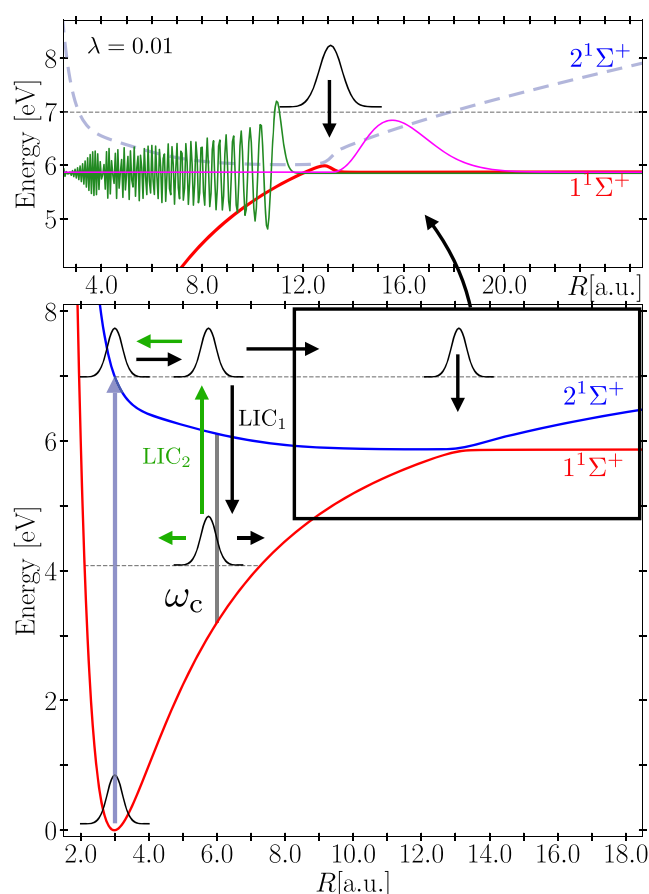


**FIG. 6.** Bottom panel: undressed potential energy curves for the lowest two  $\Sigma^+$  states of LiF, ground  $|g\rangle$  and excited  $|e\rangle$ . The covalent and ionic states show an avoided crossing at  $R = 13.1$  a.u. with a strong non-adiabatic coupling (NAC). The cavity mode frequency  $\omega_c = 2.907$  a.u. produces a light induced crossing (LIC) at  $R_{\text{LIC}} = 6$  a.u., where  $V_e - V_g = \hbar\omega_c$ . The ground vibrational state  $v = 0$  in the  $1^1\Sigma^+$  state is fully pumped (Franck-Condon transition) to the  $2^1\Sigma^+$  with an external laser source. The wave packet with energy  $\sim 7$  eV in the repulsive  $2^1\Sigma^+$  state moves to the right until it reaches the LIC at  $R = 6$  a.u., thus making a transition LIC<sub>1</sub> to the ground state  $1^1\Sigma^+$  with energy  $\sim 4$  eV. The surviving portion of the wave packet in  $2^1\Sigma^+$  keeps its motion until it reaches the non-adiabatic crossing at  $R = 13.1$  a.u. The portion that transfers to the ground state leads to dissociation. The wave packet bound in the ground state  $1^1\Sigma^+$  with energy 4 eV moves to and fro, and after reaching the LIC, it transfers back to the upper electronic state (LIC<sub>2</sub> process), with a partial reconstruction of the initial state and therefore reproducing a cyclic mechanism. Top panel: Blow-up of the region with the avoided crossing at 13 eV when the potential energy curves are modified by the dipole self-energy term in the full Rabi model for a strong coupling  $\lambda = 0.01$ . The highest vibrational bound state (solid green line) and the lowest continuum state (solid magenta line) indicate that the potential barrier reduces the vibrational probability density at the NAC.

to the dipole term  $\lambda\omega_c x\mu_{ij}(R)\cos\theta$ . For simplicity, we refer to the molecular potential energy curves in Fig. 6 to explain the full polariton dynamics. As explained in detail in our previous works, the LIC acts at  $R_{\text{LIC}} = 6$  a.u. with a first splitting of the wave packet, with a branching ratio that depends on the radiative coupling parameter

$\lambda$ . For strong coupling, the LIC<sub>1</sub> transition produces a vibrational bound wave packet in the ground state  $1^1\Sigma^+$  with energy  $E \sim 4$  eV, which keeps its initial momentum to move toward the right turning point. The reflected wave packet reaches again the LIC and it splits again, with a portion being transferred back to the excited  $2^1\Sigma^+$  state (LIC<sub>2</sub> process), thus partially reconstructing the initial wave packet at 7 eV, and a new cycle starts again. The wave packet that remains in the excited state  $2^1\Sigma^+$  after the LIC<sub>1</sub> split continues its motion to reach the NAC at  $R_{\text{NAC}} = 13.1$  a.u. with a second non-radiative transfer to the ground state, this time leading to dissociation. In this work, we are not concerned with dissociation yields but with global population changes at short times within 300 fs (before removing the dissociation component in the ground state  $1^1\Sigma^+$ ).

We perform polariton propagations in LiF using the full Rabi model (including the dipole self-energy term), the Jaynes-Cummings model (before the RWA is implemented), and using a classical field  $E(t) = E_0^C \cos \omega t$ , with the above mentioned scaling  $E_0^C = 2E_0^Q \sqrt{n+1}$  for the field amplitude. We compare the results for the time evolution of the population in the  $|g\rangle$  electronic state,  $P_g(t) = \int dR dx |\phi_g(R, x, t)|^2$  (that includes both bound and dissociation probabilities). The population in the upper electronic state  $|e\rangle$  is simply  $P_e(t) = 1 - P_g(t)$ , and it is not included in the figures. In Fig. 7, we plot the results for different radiative couplings ( $\lambda = 0.001, 0.005, 0.02$ , and  $0.025$ ). For the weakest coupling  $\lambda = 0.001$ , the radiative coupling at the LIC is almost negligible but the NAC at  $R_{\text{NAC}} = 13.1$  a.u. transfer more than half of the initial population to the ground state within the time window  $t = 80$  fs–120 fs that eventually leads to dissociation. Here, the LIC plays no role, and the initial Fock state  $|0\rangle$  remains unaltered. Consequently, the three models must produce the same results. For  $\lambda = 0.005$ , the new feature at  $t \sim 30$  fs indicates that the LIC transfer is now active, but it only amounts around 10% so that most of the transfer still corresponds to the NAC. The three calculations (full Rabi, JC and classical) yield identical transfers at the LIC, which indicates that the effect of the dipole self-energy is negligible and the classical-quantum analogy works fine by simply tuning the amplitude  $E_0^C$ .

Surprisingly, the three models produce different probabilities in the non-radiative NAC transfer at  $t = 100$  fs–120 fs. While the non-adiabatic couplings do not depend upon the value of  $\lambda$ , the potential energy surfaces do. The dipole moments (both permanent and transitional) are important in the NAC region (see Fig. 1 in Ref. 29). The LIC transfer is mostly effective at  $R_{\text{LIC}} = 6$  a.u. but due to the  $R$ -variation of dipoles  $\mu_{ij}(R)$ , there is a LIC wide region, not a simple point. In addition, the effective 2D potential energy surfaces  $V_i(R) + \frac{1}{2}\lambda^2[\hat{\mu}(R)]_{ii}^2 + \frac{1}{2}\omega_c^2 x^2 + \lambda\omega_c x\mu_{ii}(R)$  depend on the product of dipole moments  $\hat{\mu}\hat{x}$  and the dipole self-energy term on  $\hat{\mu}^2$ . The former produces  $x$ -asymmetry in the 2D surface (see graphical abstract in Ref. 29), and the latter produces modifications on the energies, specifically in the form of a barrier potential close to the  $R_{\text{NAC}}$  (see the blow-up of the inset in Fig. 6). These subtleties in the 2D- $(R, x)$  calculations make the difference with the classical calculation (which is a 1D- $R$  calculation), not because of the LIC but because of the slight modification of the landscape of potentials in the region of the non-radiative NAC. It is noteworthy that the transition at the NAC with the full Rabi model is less efficient than with the Jaynes-Cummings model, and this is attributable only to the dipole self-energy. In Fig. 6, we plot the  $1^1\Sigma^+$  curve with modifications that include the dipole self-energy term  $\frac{1}{2}\lambda^2[\hat{\mu}]^2$ . This barrier

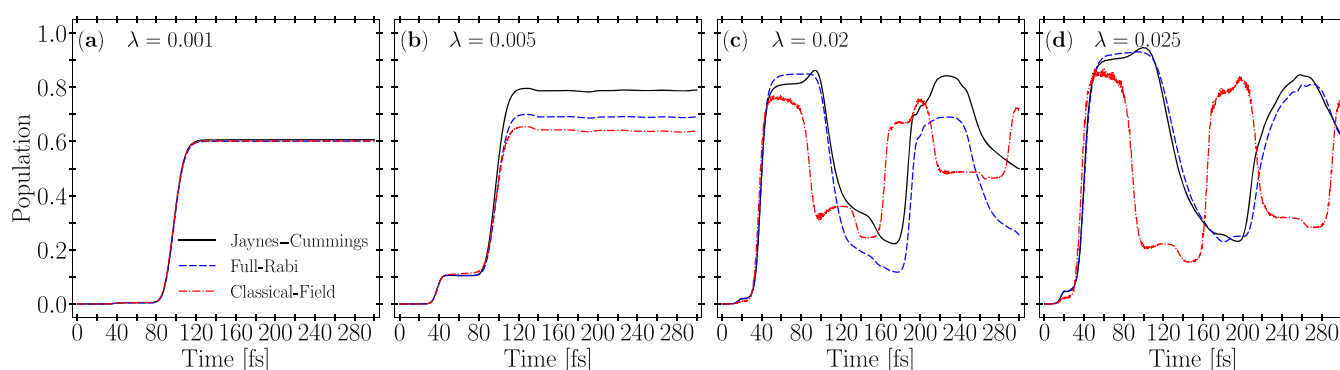


**FIG. 7.** Time dependent population of the polariton corresponding to the  $|g\rangle$  state in LiF ( $1^1\Sigma^+$  state) using three different Hamiltonians: the quantum full Rabi, the Jaynes–Cummings (without RWA), and using a classical field  $E(t)$  without rotational degrees of freedom. The results for different interaction coupling strengths: (a)  $\lambda = 0.001$  a.u., (b)  $\lambda = 0.005$  a.u., (c)  $\lambda = 0.02$  a.u., and (d)  $\lambda = 0.025$  a.u. The cavity mode frequency is  $\omega_c = 2.907$  eV. The classical field has the same frequency  $\omega = \omega_c$ , and its amplitude  $E_0^C$  is chosen as  $E_0^C = 2E_0^Q \sqrt{n + 1}$  (see text).

potential produces a void in the density of vibrational states. For instance, close to the dissociation limit, this void is more evident. In Fig. 6, we plot the highest bound vibrational state and the lowest unbound state obtained with our MCTDH basis. This effect is replicated (to a lesser extent) for higher vibrational energies. It means that the “Frank–Condon” vibrational factor associated with the NAC is less effective when the wave packet in  $2^1\Sigma^+$  approaches the position  $R_{\text{NAC}} = 13.1$  a.u. Due to the small percentage of the first LIC transfer, subsequent passages across the LIC produce minor oscillations for  $t > 120$  fs.

For strong coupling  $\lambda = 0.02$ , the first passage through the LIC<sub>1</sub> already produces a transfer to the ground state with 80%, and here, we already find notorious differences between the three models. First, the result with the classical field departs from the quantum field result. In fact, within 300 fs, the classical model shows three cycles with partial reconstructions of the initial wave packet, whereas the quantum cases are delayed around 40 fs and show two maxima instead of three. This also can be explained because of the modifications on the molecular potential energy curves induced by the quantum Hamiltonians that have a dependence on  $\lambda$ . The wave packet with the classical field moves within the 1D- $R$  unmodified potential energy curves, and the classical field with frequency  $\omega = 2.907$  eV transfers the wave packet from  $2^1\Sigma^+$  state at  $\sim 7$  eV to the  $1^1\Sigma^+$  state generating a bound state at  $\sim 4$  eV. Actually, this is the case if we observe the vibrational distribution of this bound state shown in Fig. 8, whose maximum is centered at  $E \sim 4$  eV. This peak does not shift with different field amplitudes  $E_0^C$  (or  $\lambda$ ). However, with quantum fields, the distributions are clearly shifted up in energy (the higher the coupling  $\lambda$ , the higher the vibrational energy). Ultimately, this shows that the molecular potentials  $V(R)$  are modified (they get narrower) by the permanent dipoles and the dipole self-energy term, the former being more contributing to this  $\lambda$ -shift of vibrational energy (see Fig. 8) for the values of  $\lambda$  used in this work. The bound state generated by a two-photon process is related to distributions located at  $E \sim 1$  eV. The  $\lambda$ -shift in these deep bound states is very small since the dipole moments close to the equilibrium distance are much smaller than in the region where the LIC

develops ( $R_{\text{LIC}} \sim 6$  a.u.). In addition, the two-photon transition with the classical field is supported by intermediate and final molecular vibrational states; in the quantum case, since the harmonic oscillator Fock states are included explicitly, we have one-photon transitions  $|e, 0\rangle \rightarrow |g, 1\rangle$  and from the latter final state, the transitions  $|g, 1\rangle \rightarrow |g, 2\rangle$  and  $|g, 1\rangle \rightarrow |g, 0\rangle$  [because of the non-zero permanent dipole  $\mu_{gg}(R)$ ], and this issue contributes to increase the rate with the quantum field. It must be noted that the vibrational distribution with the classical field has the highest amplitude, but it is narrower than the quantum distributions (the quantum modified potentials get narrower with a steeper profile at the LIC region), which causes that the distribution of Franck–Condon factors between the moving wave packet in  $2^1\Sigma^+$  and the vibrational stationary states in  $1^1\Sigma^+$

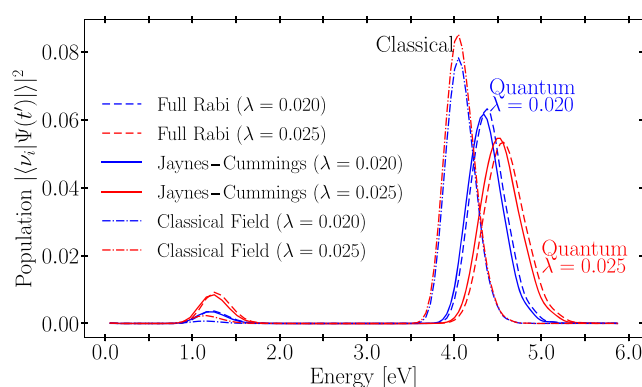


**FIG. 8.** Vibrational energy distributions of the wave packet transferred from the  $2^1\Sigma^+$  [e] state to the  $1^1\Sigma^+$  [g] state through the LIC located at  $R_{\text{LIC}} = 6$  a.u. taken at a time  $t' = 60$  fs. Distributions due to one-photon ( $E \sim 4$  eV–5 eV) and two-photon ( $E \sim 1.0$  eV–1.5 eV) transitions are in display. The results are obtained with three different Hamiltonians: full Rabi model, Jaynes–Cummings model (without RWA), and with a classical field  $E(t)$ .

be wider in energy. This effect enhances the LIC<sub>1</sub> transfer in the quantum field case.

The above mentioned  $\lambda$ -shift in the bound state vibrational distributions has crucial consequences on the subsequent dynamics. The pathway followed by the bound wave packet from the LIC<sub>1</sub> to the turning point and backward again to the LIC<sub>2</sub> is shorter in the classical field case than in the quantum case, and it explains the 40 fs delay. This implies that in the classical case, the LIC<sub>2</sub> transfer starts already at 80 fs, precisely the time at which the NAC transfer initiates, so that the former compensates the latter, although the effect of the NAC transfer is still visible around 120 fs. For the next cycle, the LIC<sub>1</sub> transfer (at 160 fs) and the NAC transfer (at 200 fs) and LIC<sub>2</sub> (at 220 fs) are more distinguishable. The two quantum field cases also show a difference at  $t = 100$  fs–170 fs, a time window in which the NAC is active making its  $|e\rangle \rightarrow |g\rangle$  transfer. Since the NAC is less efficient (as explained above) with the full Rabi model, it does not counteract the LIC<sub>2</sub>  $|g\rangle \rightarrow |e\rangle$  backtransfer. This effect amplifies in subsequent cycles. We have run many different values of  $\lambda$  to corroborate this issue, but one may find particular values of  $\lambda$  [see the plot (d) in Fig. 7 for  $\lambda = 0.025$ ] where by chance both the full Rabi and the Jaynes–Cummings models produce almost identical results due to different timings for LIC<sub>1</sub>, NAC, and LIC<sub>2</sub> transfers. The NAC transfer reaches its peak at  $t = 100$  fs–120 fs, and it is clearly appreciated in (b) and (c) in Fig. 7, but in (d), only the classical case shows a clear NAC peak, whereas the NAC peak in the quantum cases is rapidly eroded by the LIC<sub>2</sub> process (in this case, most of the population is in the  $|g\rangle$  bound state with little contribution of the  $|e\rangle \rightarrow |g\rangle$  NAC transfer). Given that LIC<sub>2</sub> is dominant from 120 fs to 200 fs, both quantum cases produce similar population yields. This case (d) even shows that the yields with the classical and quantum fields may be completely out of phase.

Now, we discuss the effects of scaling with initial Fock states  $|n\rangle$  and the introduction of molecular rotation in the realistic case of LiF. We choose a moderate coupling  $\lambda = 0.01$ , and we perform calculations with the full Rabi model without and with rotation (here introducing as initial angular states  $J = 0, 1$ , and  $2$ ). For this value of  $\lambda$ , we can clearly distinguish the yields of the LIC<sub>1</sub> process in 40 fs–80 fs and of the NAC transfer at 120 fs [see Fig. 9(a)]. We find in LiF, the same conclusions as in our previous molecular model. When the radiative coupling intervenes, the introduction of rotation reduces the LIC transition yield with the same sequence  $P_{J=0} < P_{J=2} < P_{J=1}$  below the probability without rotation. The non-radiative NAC plays a minor role with respect to the rotation. Anyway, Fig. 9 may be misleading because it gives the impression that the NAC transfer is enhanced by the rotation. This is not the case, and this effect is just due to the conservation of probability and the population ratio  $P_e(t)/P_g(t)$  before passage across the NAC. Without rotation, the LIC<sub>1</sub> process produces a ratio  $0.6/0.4 = 1.5$  at 80 fs. For instance, with rotation and  $J = 0$  as the initial state, this ratio is  $0.9/0.1 = 9$  at 80 fs. Due to the high efficiency of the NAC, a large step is expected for  $J = 0$  [compare with the case (b) in Fig. 7]. For higher values of  $\lambda$ , the effect could be just the opposite.

Finally, in Fig. 9(b), we include several calculations to assess the Fock scaling  $\lambda_n = \lambda_0/\sqrt{n+1}$  in LiF as discussed previously with the molecular model. We have used several initial Fock states  $|n\rangle$ , with  $n = 0, 1, 2$ , and  $3$ . The computation with the vacuum state is performed with  $\lambda = 0.01$ , and the rest of calculations are carried out with the corresponding scaled  $\lambda_n$ . We find that concerning the radiative

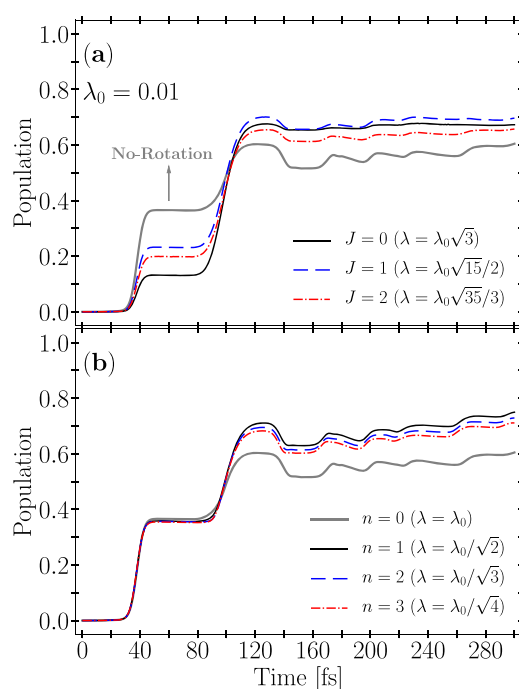


**FIG. 9.** (a) Time evolution of polariton population of the  $|g\rangle$  state in LiF, obtained with a 2D- $(R, x)$  calculation and with a 3D- $(R, x, \theta)$  calculation (including molecular rotation) with initial angular states  $J = 0, 1$ , and  $2$ , using the same coupling  $\lambda = 0.01$ . (b) Same as (a) using  $\lambda_0 = 0.01$  for the initial Fock state  $|0\rangle$  and scaled  $\lambda_n = \lambda_0/\sqrt{n+1}$  for the initial Fock state  $|n\rangle$ . All the results obtained with a full Rabi model.

LIC<sub>1</sub> and LIC<sub>2</sub>, the scaling is fulfilled. However, it must be noted that although the NAC is non-radiative and it does not follow the photon scaling, the changes in  $\lambda_n$  produce non-linear effects on the potential energy curves in the region of the NAC that eventually reflect on the populations for different  $n$  beyond the NAC. This approximate scaling worsens for higher  $\lambda$ 's. In realistic molecules where radiative and non-radiative couplings are the rule, the application of scaling rules must be thus limited to short time propagations and in time-windows where a radiative transfer dominates. Nevertheless, to prepare pure Fock states in cavity QED experiments is at present very difficult to achieve. It is more plausible to pump the cavity with an external laser source, a method that produces a coherent state that may be used as initial radiation state together with the prepared molecular state. However, scaling laws with coherent states (in terms of the different average photon numbers) are still unknown (in any) due to the high non-linearities involved.

## V. CONCLUSIONS

We have explored several issues in molecular polariton photodynamics: first, the classical–quantum analogy by using classical fields  $E(t)$  in the long-wavelength approximation and the interaction term in the length gauge  $\hat{\mu} \cdot E(t)$  and by using a Jaynes–Cummings

model or a full quantum (Pauli–Fierz) Rabi Hamiltonian. Both classical and quantum fields provide the same yield as long as the initial radiation quantum state is represented by a Fock state, and the excitation manifold is preserved because the RWA is fulfilled for weak or strong coupling regimes. In this regime, where the Jaynes–Cummings model is satisfied, the same photodynamics is obtained by using different initial Fock states  $|n\rangle$  but scaled couplings  $\lambda_n = \lambda_0/\sqrt{n+1}$ . In polar molecules, the role played by the permanent dipoles for large interaction couplings due to the modification of the landscape of polariton potential energy surfaces is stressed. In this work, we have represented quantum light in coordinate representation  $x$ , and we dealt with diatomic molecules with a nuclear degree of freedom  $R$ . Permanent dipole moments  $\sim \lambda \hat{\mu}_{ii}(R) \hat{x}$  produce asymmetries along the  $x$  direction in  $(R, x)$  potentials, and the dipole self-energy  $\frac{1}{2} \lambda^2 \hat{\mu}^2(R)$  modifies the potentials along  $R$ . For large coupling  $\lambda$ , these distortions in the potentials may change the photodynamics dramatically. Finally, we find that the introduction of molecular rotation in diatoms, which induces the presence of light-induced conical intersections in the 3D- $(R, x, \theta)$  potential energy surfaces, does not enhance radiation transition yields in comparison to 2D- $(R, x)$  yields.

We have explored these issues in a diatomic molecular model (that allows for fast calculations) containing the typical ingredients of realistic molecules such as LiF for which full *ab initio* calculations can be performed for the structure (using MOLPRO) and photodynamics (using MCTDH). At variance with the proposed model, LiF has a strong non-adiabatic coupling in an avoided crossing. In this particular case, both permanent dipole and transition dipole moments are non-zero in the region of the ionic-covalent crossing. Although this interaction is non-radiative, permanent dipoles and self-energy terms modify the potential surfaces in this transitional region for large  $\lambda$  couplings, which prevents the system from any scaling.

We have addressed these properties for an isolated molecule within a cavity, and at present, this is more a formal academic fundamental problem than a realm in laboratories. A regimen of strong and ultrastrong couplings may be usually achieved for a large ensemble of molecules. Instead of a Jaynes–Cummings model, one requires collective models such as Tavis–Cummings or Holstein–Tavis–Cummings. Scaling and rotational effects and the role of permanent dipoles in these collectives (along with dissipation effects) are yet to be explored.

## ACKNOWLEDGMENTS

J.L.S.-V thanks financial support from Vicerrectoría de Investigación at Universidad de Antioquia, Colombia, through Estrategia de Sostenibilidad and CODI Convocatoria Programática Project No. 2017-16348. J.F.T. is supported by Agencia Nacional de Investigación y Desarrollo (ANID), Chile, through the Postdoctoral Fellowship Grant No. 3200565.

## DATA AVAILABILITY

The data that support the findings of this study are available from the corresponding author upon reasonable request.

## REFERENCES

- 1 F. Herrera and F. C. Spano, “Cavity-controlled chemistry in molecular ensembles,” *Phys. Rev. Lett.* **116**, 238301 (2016).
- 2 M. Kowalewski, K. Bennett, and S. Mukamel, “Non-adiabatic dynamics of molecules in optical cavities,” *J. Chem. Phys.* **144**, 054309 (2016).
- 3 M. Kowalewski, K. Bennett, and S. Mukamel, “Cavity femtochemistry: Manipulating nonadiabatic dynamics at avoided crossings,” *J. Phys. Chem. Lett.* **7**, 2050–2054 (2016).
- 4 M. Kowalewski and S. Mukamel, “Manipulating molecules with quantum light,” *Proc. Natl. Acad. Sci. U. S. A.* **114**, 3278–3280 (2017).
- 5 J. Flick, M. Ruggenthaler, H. Appel, and A. Rubio, “Atoms and molecules in cavities, from weak to strong coupling in quantum-electrodynamics (QED) chemistry,” *Proc. Natl. Acad. Sci. U. S. A.* **114**, 3026–3034 (2017).
- 6 J. Feist, J. Galego, and F. J. García-Vidal, “Polaritonic chemistry with organic molecules,” *ACS Photonics* **5**, 205–216 (2018).
- 7 R. F. Ribeiro, L. A. Martínez-Martínez, M. Du, J. Campos-González-Angulo, and J. Yuen-Zhou, “Polariton chemistry: Controlling molecular dynamics with optical cavities,” *Chem. Sci.* **9**, 6325–6339 (2018).
- 8 F. Herrera and J. Owrutsky, “Molecular polaritons for controlling chemistry with quantum optics,” *J. Chem. Phys.* **152**, 100902 (2020).
- 9 J. P. Long and B. S. Simpkins, “Coherent coupling between a molecular vibration and Fabry–Perot optical cavity to give hybridized states in the strong coupling limit,” *ACS Photonics* **2**, 130–136 (2015).
- 10 M. Muallem, A. Palatnik, G. D. Nessim, and Y. R. Tischler, “Strong light-matter coupling and hybridization of molecular vibrations in a low-loss infrared microcavity,” *J. Phys. Chem. Lett.* **7**, 2002–2008 (2016).
- 11 J. George, T. Chervy, A. Shalabney, E. Devaux, H. Hiura, C. Genet, and T. W. Ebbesen, “Multiple Rabi splittings under ultrastrong vibrational coupling,” *Phys. Rev. Lett.* **117**, 153601 (2016).
- 12 T. W. Ebbesen, “Hybrid light–matter states in a molecular and material science perspective,” *Acc. Chem. Res.* **49**, 2403–2412 (2016).
- 13 W. Ahn, I. Vurgaftman, A. D. Dunkelberger, J. C. Owrutsky, and B. S. Simpkins, “Vibrational strong coupling controlled by spatial distribution of molecules within the optical cavity,” *ACS Photonics* **5**, 158–166 (2018).
- 14 R. Chikkaraddy, B. de Nijs, F. Benz, S. J. Barrow, O. A. Scherman, E. Rosta, A. Demetriadou, P. Fox, O. Hess, and J. J. Baumberg, “Single-molecule strong coupling at room temperature in plasmonic nanocavities,” *Nature* **535**, 127–130 (2016).
- 15 O. Vendrell, “Collective Jahn–Teller interactions through light-matter coupling in a cavity,” *Phys. Rev. Lett.* **121**, 253001 (2018).
- 16 I. S. Ulusoy, J. A. Gomez, and O. Vendrell, “Modifying the nonradiative decay dynamics through conical intersections via collective coupling to a cavity mode,” *J. Phys. Chem. A* **123**, 8832–8844 (2019).
- 17 R. H. Dicke, “Coherence in spontaneous radiation processes,” *Phys. Rev.* **93**, 99–110 (1954).
- 18 M. Tavis and F. W. Cummings, “Exact solution for an  $N$ -molecule–Radiation-field Hamiltonian,” *Phys. Rev.* **170**, 379–384 (1968).
- 19 R. E. F. Silva, J. del Pino, F. J. García-Vidal, and J. Feist, “Polaritonic molecular clock for all-optical ultrafast imaging of wavepacket dynamics without probe pulses,” *Nat. Commun.* **11**, 1423 (2020).
- 20 I. S. Ulusoy and O. Vendrell, “Dynamics and spectroscopy of molecular ensembles in a lossy microcavity,” *J. Chem. Phys.* **153**, 044108 (2020).
- 21 S. Felicetti, J. Fregoni, T. Schnappinger, S. Reiter, R. de Vivie-Riedle, and J. Feist, “Photoprotecting uracil by coupling with lossy nanocavities,” *J. Phys. Chem. Lett.* **11**, 8810–8818 (2020).
- 22 P. Antoniou, F. Suchanek, J. F. Varner, and J. J. Foley, “Role of cavity losses on nonadiabatic couplings and dynamics in polaritonic chemistry,” *J. Phys. Chem. Lett.* **11**, 9063–9069 (2020).
- 23 N. Moiseyev, M. Šindelka, and L. S. Cederbaum, “Laser-induced conical intersections in molecular optical lattices,” *J. Phys. B: At., Mol. Opt. Phys.* **41**, 221001 (2008).
- 24 A. Csehi, G. J. Halász, L. S. Cederbaum, and Á. Vibók, “Competition between light-induced and intrinsic nonadiabatic phenomena in diatomics,” *J. Phys. Chem. Lett.* **8**, 1624–1630 (2017).



- <sup>25</sup>T. Szidarovszky, G. J. Halász, A. G. Császár, L. S. Cederbaum, and Á. Vibók, "Direct signatures of light-induced conical intersections on the field-dressed spectrum of Na<sub>2</sub>," *J. Phys. Chem. Lett.* **9**, 2739–2745 (2018).
- <sup>26</sup>T. Szidarovszky, G. J. Halász, A. G. Császár, L. S. Cederbaum, and Á. Vibók, "Conical intersections induced by quantum light: Field-dressed spectra from the weak to the ultrastrong coupling regimes," *J. Phys. Chem. Lett.* **9**, 6215–6223 (2018).
- <sup>27</sup>A. Csehi, G. J. Halász, L. S. Cederbaum, and Á. Vibók, "Intrinsic and light-induced nonadiabatic phenomena in the NaI molecule," *Phys. Chem. Chem. Phys.* **19**, 19656–19664 (2017).
- <sup>28</sup>A. Csehi, M. Kowalewski, G. J. Halász, and Á. Vibók, "Ultrafast dynamics in the vicinity of quantum light-induced conical intersections," *New J. Phys.* **21**, 093040 (2019).
- <sup>29</sup>J. F. Triana, D. Peláez, and J. L. Sanz-Vicario, "Entangled photonic-nuclear molecular dynamics of LiF in quantum optical cavities," *J. Phys. Chem. A* **122**, 2266–2278 (2018).
- <sup>30</sup>J. F. Triana and J. L. Sanz-Vicario, "Revealing the presence of potential crossings in diatomics induced by quantum cavity radiation," *Phys. Rev. Lett.* **122**, 063603 (2019).
- <sup>31</sup>A. Csehi, Á. Vibók, G. J. Halász, and M. Kowalewski, "Quantum control with quantum light of molecular nonadiabaticity," *Phys. Rev. A* **100**, 053421 (2019).
- <sup>32</sup>A. Mandal, S. Montillo Vega, and P. Huo, "Polarized Fock states and the dynamical Casimir effect in molecular cavity quantum electrodynamics," *J. Phys. Chem. Lett.* **11**, 9215–9223 (2020).
- <sup>33</sup>J. B. Pérez-Sánchez and J. Yuen-Zhou, "Polariton assisted down-conversion of photons via nonadiabatic molecular dynamics: A molecular dynamical Casimir effect," *J. Phys. Chem. Lett.* **11**, 152–159 (2020).
- <sup>34</sup>J. F. Triana, F. J. Hernández, and F. Herrera, "The shape of the electric dipole function determines the sub-picosecond dynamics of anharmonic vibrational polaritons," *J. Chem. Phys.* **152**, 234111 (2020).
- <sup>35</sup>C. Schäfer, M. Ruggenthaler, V. Rokaj, and A. Rubio, "Relevance of the quadratic diamagnetic and self-polarization terms in cavity quantum electrodynamics," *ACS Photonics* **7**, 975–990 (2020).
- <sup>36</sup>J. Feist, A. I. Fernández-Domínguez, and F. J. García-Vidal, "Macroscopic QED for quantum nanophotonics: Emitter-centered modes as a minimal basis for multiemitter problems," *Nanophotonics* **10**, 477–489 (2021).
- <sup>37</sup>C. Gerry and P. Knight, *Introductory Quantum Optics* (Cambridge University Press, Cambridge, 2005).
- <sup>38</sup>G. J. Halász, M. Šindelka, N. Moiseyev, L. S. Cederbaum, and Á. Vibók, "Light-induced conical intersections: Topological phase, wave packet dynamics, and molecular alignment," *J. Phys. Chem. A* **116**, 2636–2643 (2012).
- <sup>39</sup>H.-D. Meyer, U. Manthe, and L. S. Cederbaum, "The multi-configurational time-dependent Hartree approach," *Chem. Phys. Lett.* **165**, 73–78 (1990).
- <sup>40</sup>M. Beck, A. Jackle, G. Worth, and H.-D. Meyer, "The multiconfiguration time-dependent Hartree (MCTDH) method: A highly efficient algorithm for propagating wavepackets," *Phys. Rep.* **324**, 1–105 (2000).
- <sup>41</sup>G. Worth, M. Beck, A. Jäckle, and H. Meyer, The MCTDH Package, version 8.4, 2007, <http://mctdh.uni-hd.de>.
- <sup>42</sup>H. Meyer, F. Gatti, and G. Worth, *Multidimensional Quantum Dynamics: MCTDH Theory and Applications* (John Wiley & Sons, 2009).
- <sup>43</sup>C.-C. Shu, K.-J. Yuan, D. Dong, I. R. Petersen, and A. D. Bandrauk, "Identifying strong-field effects in indirect photofragmentation reactions," *J. Phys. Chem. Lett.* **8**, 1–6 (2017).
- <sup>44</sup>H.-J. Werner *et al.*, Molpro, version 2015.1, a package of *ab initio* programs, 2015, <http://www.molpro.net>.